6 AFM Nanoindentation Method: Geometrical Effects of the Indenter Tip

Lorenzo Calabri · Nicola Pugno · Sergio Valeri

Abstract. Atomic force microscopy (AFM) nanoindentation is presently not that widespread for the study of mechanical properties of materials at the nanoscale. "Nanoindenter" machines have greater accuracy and are presently more standardized. However, AFM could provide interesting features such as imaging the indentation impression right after the application of load. The AFM has, in fact, become an increasingly popular tool for characterizing surfaces and thin films of many different types of materials and recent developments have led to the utilization of the AFM as a nanoindentation device, increasing the accuracy of this machine.

In this work a new method for nanoindentation via AFM is proposed. It allows hardness measurement with standard sharp AFM probes and a simultaneous high-resolution imaging (which is not achievable with standard indenters – *Cube Corner* and *Berkovich*). How the shape of the indenter and the tip radius of curvature affect the hardness measurement at the nanoscale is herein analyzed with three different approaches: experiments, numerical simulations, and theoretical models. In particular the effect of the tip radius of curvature, which is not negligible for the real indenters, has been considered both in the nature of the indentation process, and in the practice of imaging via AFM.

A complete theoretical model has been developed and it includes the effect of the tip radius of curvature as well as the variable corner angle. Through this model we have been able to define a correction factor C that permits us to evaluate the actual hardness of the material, once measured the actual geometry of the tip.

Key words: Nanoindentation, Atomic Force Microscopy, Finite element method, Indentation shape effect, Tip radius of curvature effect

6.1 Introduction

As defined by Fisher-Cripps indentation testing is "a simple method that consists essentially of touching the material whose mechanical properties such as elastic modulus and hardness are unknown with another material whose properties are known" [1]. Nanoindentation differs from conventional macro-indentation in the length scale of the penetration, which is of the order of nanometers rather than microns or millimeters. Over the last few years, interest in nanomechanics has grown exceptionally. In particular the mechanical properties of materials at the nanoscale have been carefully investigated from a theoretical and experimental point of view, but theoretical work strongly depends upon accurate experimental results. The nanoindentation

technique, in particular, has been extensively exploited by many researchers all over the world in order to study hardness, Young's modulus, and other mechanical properties of thin films and coatings such as the strain-hardening exponent, fracture toughness (for brittle materials), and viscoelastic properties [2–5]. The technique has also been thoroughly investigated in order to understand its main features at the nanoscale [6].

The idea of nanoindentation, in fact, arose from the necessity to measure the mechanical properties of very small volumes of materials. In principle, if a very sharp tip is used, the volume of material that is tested can be made arbitrarily small but in this case it is very difficult to determine the indentation area. In a conventional hardness test, in fact, the characteristic contact area of the indentation is calculated from direct measurements of the residual impression left in the specimen surface. In a nanoindentation test, the size of the residual impression is on the sub-micrometer range and too small to be conventionally measured (optical microscopy). The hardness is in fact defined as the ratio between the maximum applied load (*Pmax* – easily measurable during the indentation) and the projected area of the indentation impression (A_p – not measurable directly by conventional methods). This area can be evaluated measuring the depth of indentation into the surface, which provides an indirect measurement of the contact area, knowing the actual geometry of the indenter. For this reason nanoindentation can be considered a special case of the more general Depth Sensing Indentation (*DSI*) methods [7–10]. In particular most of the recent studies concerning material nanohardness, are based on the analysis of the load-displacement curves resulting from the nanoindentation test using the Oliver and Pharr (O-P) method [8, 9, 11]. The O-P method allows hardness measurement without imaging the indentation impression, since it establishes a relationship between the projected area of the indentation impression (A_p), the maximum depth of indentation ($h_{\max}$), and the initial unloading stiffness (S), where $h_{\max}$ and S are both measurable from the load-displacement curve (Fig. 6.1 [9]).

The atomic force microscopy (AFM) approach to nanoindentation [5, 12, 13] on the contrary permits a direct measurement of the projected area of the indentation

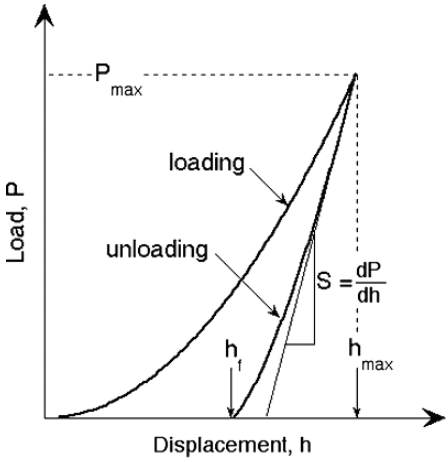

Fig. 6.1. Schematic illustration of indentation load-displacement data [9] showing important measured parameters. [Reprinted from [9], Copyright (2004) Materials Research Society. Reproduced with permission.]

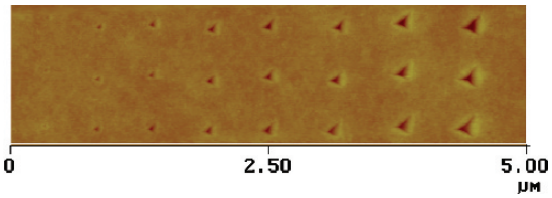

Fig. 6.2. AFM image of the plastic impressions [13] remaining in the BCB material after indentation (height scale is 0 to 20 nm from *black* to *white*). [Reprinted from [13], Copyright (2001) reproduced with permission.]

impression. As a matter of fact, AFM could provide interesting features such as imaging the indentation impression right after the application of load (Fig. 6.2, [13]).

The AFM has become an increasingly popular tool for characterizing surfaces and thin films of many different types of materials and recent developments have led to the utilization of the AFM as a nanoindentation device. During operation of the AFM in indentation mode, the probe tip is first lowered into contact with the sample, then indented into the surface, and finally lifted off the sample surface. AFM software has been modified and diamond-tipped probes have been developed (Fig. 6.3.) specifically for indenting and scratching materials with nanoscale spatial resolution. The software modification allows the surface to be imaged in tapping mode immediately before and after indentation.

With this approach it is thus possible to obtain the exact morphology of the indentation impression with high resolution at the nanoscale (Fig. 6.2) and to directly measure the actual value of the projected area A_p. This approach allows us also to consider the presence of piled-up material (Fig. 6.4 [14]), which is a major topic for indentation at the nanoscale [14, 15]. The pile-up effect is usually neglected with the O-P approach and leads to an overestimation of the hardness value [16–18]. Beegan et al. [14] used, in the case reported in Fig. 6.4, specific software (Matlab®) in order

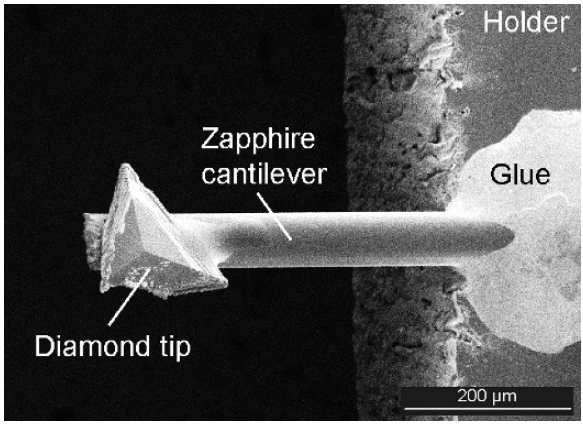

Fig. 6.3. SEM image of an AFM diamond-tipped probe (Cube Corner indenter) customized specifically for indenting and scratching

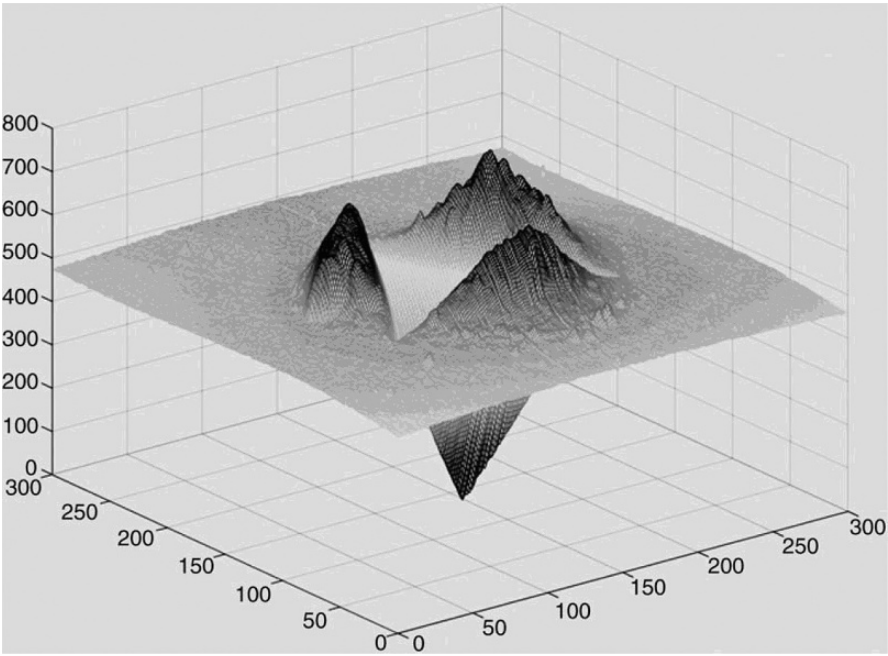

Fig. 6.4. Matlab® mesh surface plot of 40-mN indent in 750-nm Cu film. [Reprinted from [14], Copyright (2005), with permission from Elsevier.]

to characterize and precisely quantify the amount of piled-up material, exploiting 3D images obtained by AFM investigation.

Hardness, as previously mentioned, is the mean pressure that a material bears under load. This parameter is only "nominally" an intrinsic constant factor and it is experimentally affected by several geometrical uncertainties, such as penetration depth, size and shape of the indenter [19–22]. Nix et al. in an early work about nanoindentation [20], illustrate the size effects in crystalline materials, showing that the hardness of a material strongly depends upon depth of indentation, tending asymptotically to the macroscopic hardness of the material (Fig. 6.5, [20]).

Much of the early work on indentation was reviewed by Mott [23]. Afterwards Ashby [24] proposed that geometrically necessary dislocations [25] would lead to an increase in hardness measured by a flat punch. The problem of a conical indenter has been thoroughly investigated by Nix et al. [20], showing a consistent agreement with micro-indentation experiments. However, recent results that cover a greater range of depths show only partial [21, 26] or no agreement [27] with this model [20]. Thus, the model initially proposed by Nix et al. was extended by Swadener et al. [21] in order to cover a greater range of depth (Fig. 6.6, [21]) and also to treat indenters with different sizes and shapes. The results were compared with micro-indentation experiments, but limitations for small depths of indentation were observed, as pointed out by the same authors. In the last few years a new model capable of matching as limit cases all the discussed indentation laws, simultaneously capturing the deviation

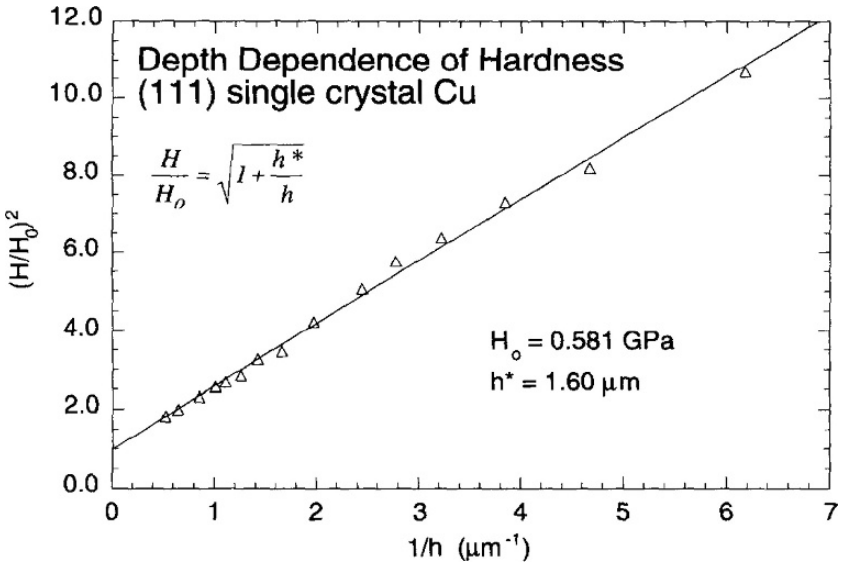

Fig. 6.5. Depth dependence of the hardness of (111) single crystal copper plotted according to the equation reported in the graph. [Reprinted from [20], Copyright (1998), with permission from Elsevier.]

observed towards the nanoscale, has been proposed by Pugno [28] and will be thoroughly discussed in Sect. 6.4.

In this chapter the geometrical uncertainties related to the indenter tip (shape and radius of curvature) are investigated in order to find a way to compensate for these effects. In particular, considerations about the tip shape, in terms of tip corner angle, have been deduced in order to understand what the effect of indenter geometry is on the material hardness evaluation. Thanks to this approach a new method for nanoindentation is proposed. It allows hardness measurement with standard sharp AFM probes (thus with variable corner angle); the use of these probes enables a simultaneous high-resolution imaging (which is not easily achievable with standard indenters – *Cube Corner* and *Berkovich*). How the shape of the indenter [19] and the tip radius of curvature [29] affect the hardness measurement is herein analyzed to find a relationship between the measured hardness of a material, the corner angle of the pyramidal indenter, and its tip radius of curvature. To experimentally understand this effect a photoresist material (*Microposit s1813 photo resists*) has been indented with Focused Ion Beam (FIB) nanofabricated probes with different corner angles [19]. We then compared the results obtained experimentally with those obtained by numerical simulations and by theoretical models [28].

The comparison between these three approaches reveals a good agreement in the hardness behavior even if an overestimation of the experimental results was noticed at small corner angles [19]. This is related to the tip radius of curvature of the real indenters, which is not negligible and affects the experimental results, both in the nature of the experimental procedure, and then in the process of imaging with AFM.

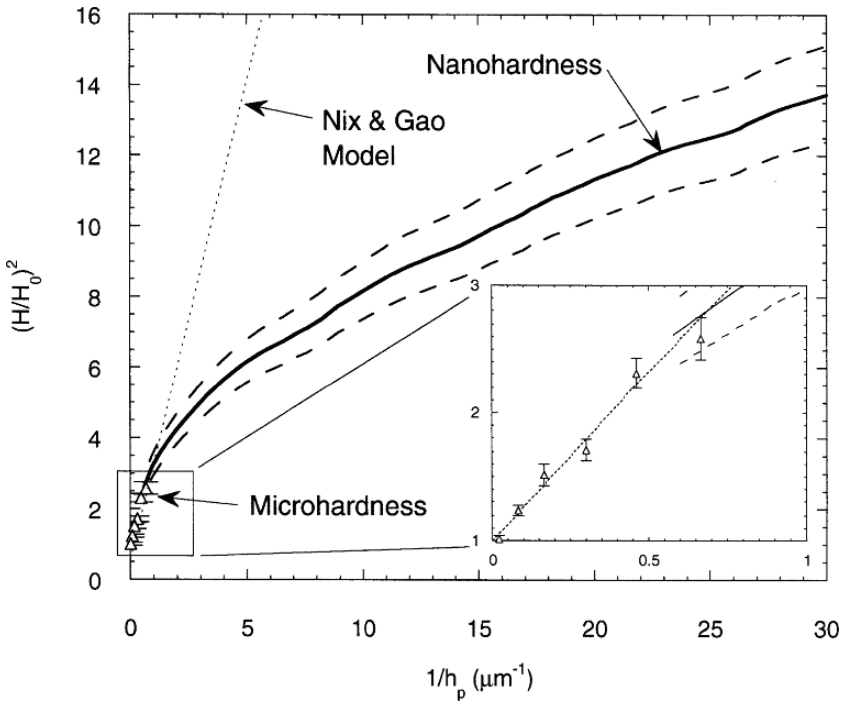

Fig. 6.6. Indentation size effect in annealed iridium measured with a Berkovich indenter (Δ and *solid line*) and comparison of experiments with the Nix et al. [20] model for $H_0 = 2.5$ GPa and $h_p = 2.6\,\mu$m (*dotted line*).The *dashed lines* represent $+$ and $-$ one standard deviation of the nanohardness data. [Reprinted from [21], Copyright (2002), with permission from Elsevier.]

The presence of a non-zero tip radius of curvature is ascribable to wear during the indent-imaging process or to manufacturing defects. It could affect the indentation process because the indenter, no longer ideal, will deform the specimen with a different geometry. However, it could also affect the process of imaging, as long as the non-ideal tip interacts with the morphology, convoluting the asperities depending on its actual shape. For this reason the theoretical and numerical models have been modified in order to compensate for these effects and to obtain a closer match between experimental and numerical approaches. In this way we were also able to define a correction factor C which permits us to evaluate the actual hardness of the material, filtering the experimental data.

6.2 Experimental Configuration

In this section the experimental approach proposed by the authors in a previous work [19] is reviewed and extended.

Table 6.1. Mechanical properties of the specimen material (photoresist). [Reprinted from [19], Copyright (2007), with permission from IoP.]

Mechanical property	Reference value
Microhardness	$\sim$ 200 MPa
Ultimate tensile strength	51.2 MPa
Yield tensile strength	43 MPa
Elongation at break	0.6%
Young's modulus	8 GPa
Poisson's ratio	0.33

The set of indenters used for the nanoindentation experimental analysis are commercial silicon AFM tips, in particular we used *MPP-11100-Tap300 Metrology Probes* from *Veeco*®. The commercial silicon AFM tips are easy to find, cheap and reshapable with the FIB nanofabrication process. These kinds of tips are silicon made and consequently they could not provide a high mechanical profile in terms of hardness and non-deformability. For this reason we decided to use them to indent a soft substrate in order to keep a high ratio between the hardness of the indenter and the hardness of the sample. In this way the silicon tips, even if they provide a poor hardness value, will be basically non-deformable when pressed on the selected soft material. The substrate we used is a photoresist material, namely a *Microposit s1813 photo resists* by *Shipley*®. It is a *positive* photoresist based on a *NOVOLAC* polymer. Its mechanical properties are reported in Table 6.1 [19]. This material is ideal for this kind of study, because it is very soft, thus easy to indent with a silicon tip, and at the same time it is very flat, allowing an accurate measurement of the indentation projected area.

6.2.1 FIB Nanofabrication

The pristine geometry of the probe tip is a quadratic pyramid (Fig. 6.7a,b). As reported in the Veeco® probes catalogue the characteristic geometry of the tip is listed in the table inset in Fig. 6.7b.

In this work, in order to obtain a set of indenters with a variable corner angle, we functionalized the pristine probes with a FIB apparatus in order to transform them into a triangular pyramid (as nanoindenters usually are). The FIB system is a Dual Beam machine (*FEI StrataTM DB 235*) combining a high-resolution FIB column equipped with a Ga Liquid Metal Ion Source (LMIS) and a SEM column equipped with a Schottky Field Emission Gun (SFEG) electron source. FIB offers the ability to design, sculpt or pattern nano- and micro-structures on different materials with spatial resolution down to 20 nm.

By means of the FIB machine we proceeded in cutting the tip with a plane positioned with a proper different orientation. In this way we utilized two pristine faces of

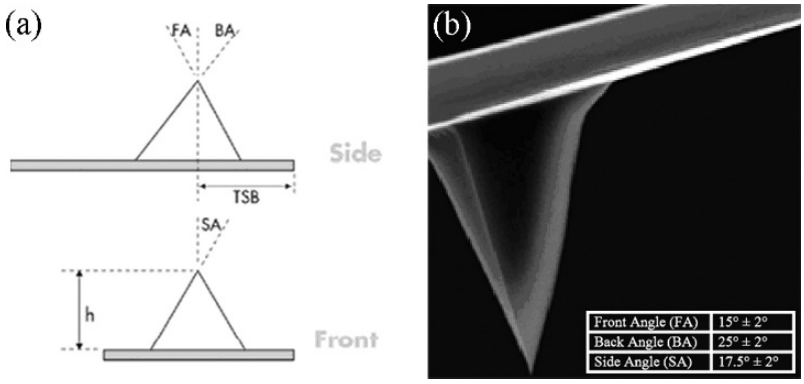

Fig. 6.7. (**a**) Schematic of the tip geometry (from Veeco® probes catalogue); (**b**) image of the pristine probe (from Veeco® probes catalogue)

the original tip and we just created the third face. In Fig. 6.8 is reported the reshaping procedure step by step [19].

With this procedure we realized three different indenters. In Fig. 6.9 the SEM images of the three probes obtained by FIB nanofabrication are reported [19]. The orientation of the cutting planes is an important feature in order to fabricate a tip that approaches the sample perpendicularly to the surface. To obtain these geometries we always consider the 12° angle of the AFM probe holder (Fig. 6.8b). The second probe is obtained cutting the tip with three different planes (there was no chance in fact to utilize any pristine face of the original probe) and the shape was completely recreated (Fig. 6.9b).

In Fig. 6.10 one can see the final shape of customized probe n°1 [19], observed with the SEM microscope (Fig. 6.10a,b) and with AFM (Fig. 6.10c) using a calibration grid composed of an array of sharp tips (test grating *TGT1 – NT-MDT*®).

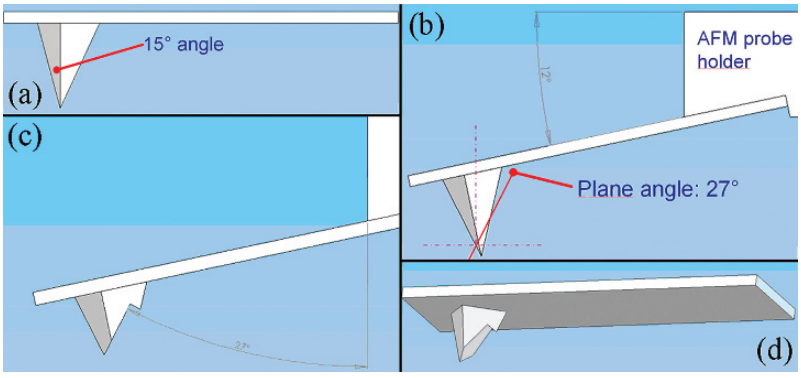

Fig. 6.8. (**a**) Probe pristine geometry; (**b**) position of the cutting plane; (**c**) tip profile after the reshaping phase; (**d**) axonometric projection of the customized probe. [Reprinted from [19], Copyright (2007), with permission from IoP.]

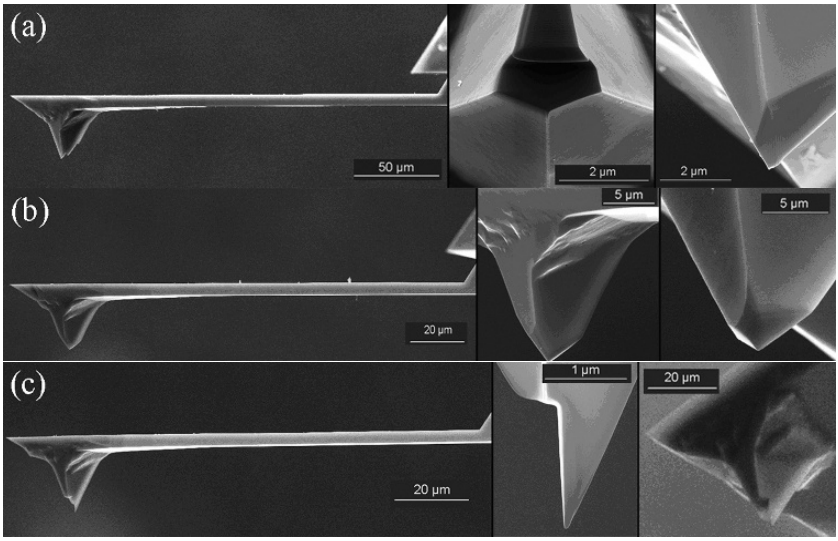

Fig. 6.9. SEM images of the customized probes [19]: (**a**) indenter n°1 – equivalent corner angle of 62°; (**b**) indenter n°2 – equivalent corner angle of 97°; (**c**) indenter n°3 – equivalent corner angle of 25. [Reprinted from [19], Copyright (2007), with permission from IoP.]

The final shape of the indenters is a triangular pyramid with a customized geometry. To codify the new geometry of the nanofabricated probes the characteristic parameter which has been used is the *equivalent corner angle*. The equivalent corner angle of a triangular pyramid is defined as the corner angle of a conical indenter with the same area function. Using this kind of codification we obtained for the three functionalized indenters the angles listed in Table 6.2 [19].

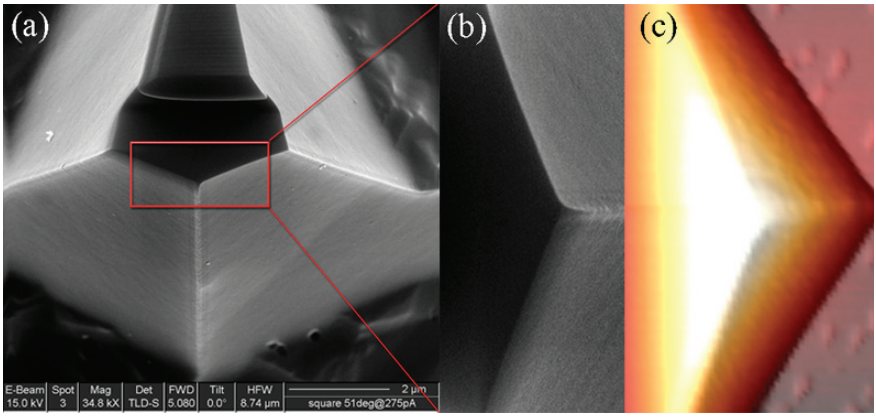

Fig. 6.10. (**a**,b) SEM images of the customized probe n°1; (**c**) AFM image on the calibration grid of the customized probe n°1 [19]. [Reprinted from [19], Copyright (2007), with permission from IoP.]

Table 6.2. Equivalent corner angles of the nanofabricated probes. [Reprinted from [19], Copyright (2007), with permission from IoP.]

Indenter	Equivalent corner angle [°]
Probe n°1	62
Probe n°2	97
Probe n°3	25

6.2.2 Tip Radius of Curvature Characterization

In the AFM indentation procedure, the radius of curvature at the tip affects the hardness measurement in two different ways: (1) it has an influence on the nature of the penetration process, as long as the indenter, no more ideal, will deform the specimen with a different geometry; (2) it affects the process of AFM imaging, as long as the non-ideal tip will interact with the morphology, convoluting the asperities depending on its actual shape. For this reason it is necessary to determine the real shape of the indenter (in terms of tip radius of curvature) in order to modify and develop the theoretical and numerical models.

This characterizing procedure, yet introduced in a previous work [29], is herein reviewed. The topography of the customized indentation tips has been obtained by a SEM microscope equipped with a SFEG electron source and also by an AFM working in tapping mode. Using the SEM we are able to directly obtain the geometry of the tip (Fig. 6.11a, [29]), although the image obtained is a 2D projection of the tip. The result achieved in this way does not concern the actual three-dimensional structure of the system, but just a planar view of it.

Using the AFM, it is in addition possible to obtain a 3D topography of the tip (Fig. 6.11b, [29]), scanning the probe on a calibration grid (test grating *TGT1 – NT-MDT®*). The image obtained in this way is three-dimensional and represents the actual shape of the indenter. Using the "Tip characterization" tool equipped with the

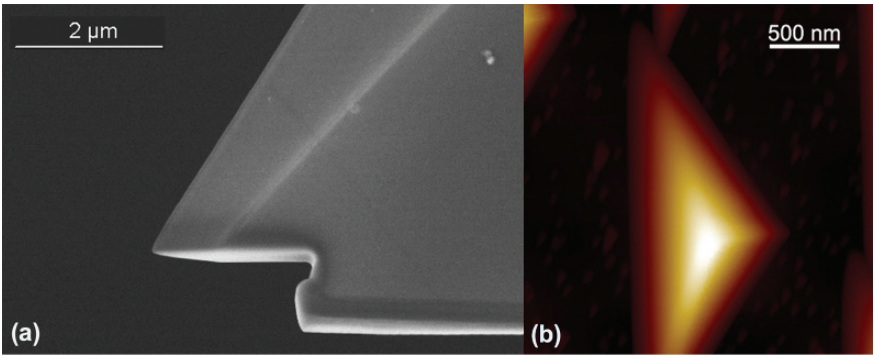

Fig. 6.11. (**a**) SEM image of the customized probe n°1; (**b**) AFM image on the calibration grid of the customized probe n°1 [29]

Table 6.3. Tip radius of curvature of the nanofabricated probes [29]

Indenter	Tip radius of curvature [nm]
Probe n°1	21
Probe n°2	26
Probe n°3	25

SPIP™ software that we used for the AFM image analysis, we are able to precisely detect the tip radius of curvature of the three customized probes used for the nanoindentation procedure (Table 6.3, [29]).

6.2.3 Nanoindentation Experimental Setup

The whole experimental analysis has been carried out using AFM nanoindentation. The instrument that we used was a *Digital Instruments EnviroScope Atomic Force Microscope* by *Veeco*®. This instrument allowed us to indent the sample and image it right after the indentation. The experiments consisted of a matrix of 25 indentations (Fig. 6.12) performed for each probe under exactly the same conditions. The indentations reported in Fig. 6.12 reveal a clear pile-up. This phenomenon is related to the material, which is very soft, and also to the geometry of the tip (decreasing the corner angle of the tip increases the plastic deformation of the material and thus its pile-up).

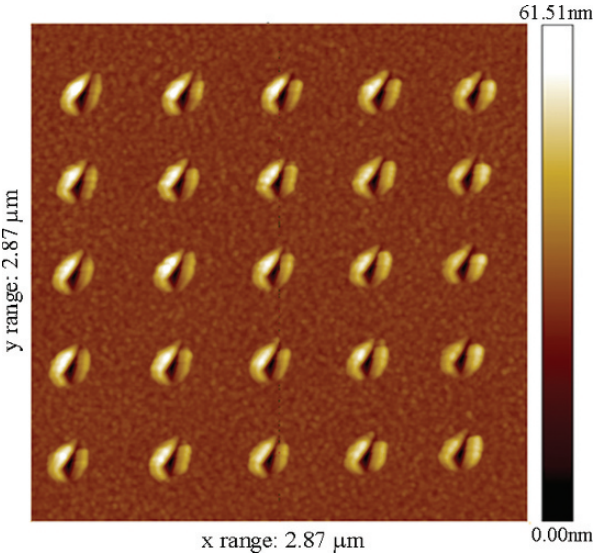

Fig. 6.12. AFM image of the indentation matrix, composed of 25 indentations, performed for each probe under exactly the same conditions

Table 6.4. Elastic spring constant and deflection sensitivity of the probes. [Reprinted from [19], Copyright (2007), with permission from IoP.]

Indenter	Spring constant [N/m]	Deflection sensitivity [nm/V]
Probe n°1	49.0	34.2
Probe n°2	35.2	34.5
Probe n°3	38.4	34.8

The load applied to the sample is 1.6 V in terms of photodetector voltage. Thus, considering the cantilever spring constant (obtained using the *Sader* approach [30, 31]) and the deflection sensitivity, we obtain a maximum load for the three indenters of about 2,000 nN.

The deflection sensitivity has been calibrated using the load-displacement curves and it corresponds to the slope of the force plot in the contact region. The deflection sensitivity is the factor that allows us to convert the cantilever deflection from volts to nanometers. The results in terms of elastic spring constant and deflection sensitivity for the three probes are reported in Table 6.4 [19].

6.3 Numerical Model

The Finite Element Method (FEM) is herein used to simulate the indentation process in order to find a numerical correlation between the hardness value and the shape of the indenter, considering also the effect of the tip radius of curvature.

In this analysis we approach the numerical model as a non-linear contact problem. Both the indenter and the specimen are considered bodies of revolution and the pyramid indenter is approximated by an axisymmetric cone (Fig. 6.13 [29]) with the same equivalent corner angle. In this way it is possible to avoid a high computing time connected with the three-dimensional nature of the problem, with no introduction of considerable errors. Using a 3-D pyramid indenter, in fact, there will be an elastic singularity at its edges, influencing the stress-strain response of only a tiny area close to these edges. On the contrary this will not affect the continuum plastic behavior of the material, with no interference in its load-deflection response [32].

In the present model it is assumed that the indenter is perfectly rigid and the test material is isotropic homogeneous, elasto-plastic with isotropic hardening behavior, obeying von Mises' yield criterion; the material was assumed to be elastic-fully plastic, thus with no strain hardening [19, 29]. This is an acceptable hypothesis, since the material is a polymer-based photoresist which presents a perfectly plastic regime characterized by a constant yield stress [33].

The indentation process is simulated moving the indenter with a downward-upward displacement (100 nm). This causes the indenter to push into the surface and then release, until it is free of contact with the specimen.

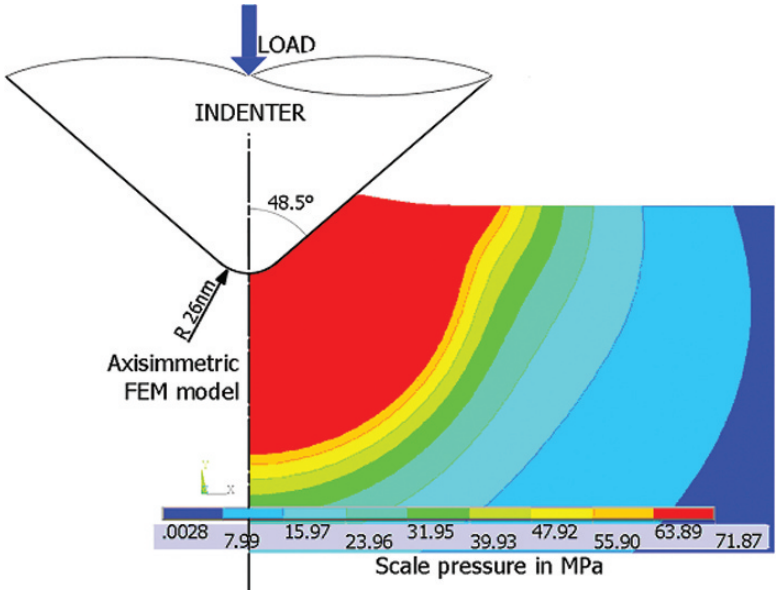

Fig. 6.13. Stress distribution in the indentation model for the probe n°2 (corner angle = 97°); the *vertical blue arrow* represents the applied load direction during the indentation process [29]

The indenter is modeled using the equivalent corner angles designed for the customized probes (62, 97, and 25° – Table 6.2) and using the tip radius of curvature obtained from the tip characterization (21, 26, and 25 nm – Table 6.3).

6.4 Theoretical Model: A Shape/Size-Effect Law for Nanoindentation

In this section the approach proposed by Pugno [28] is reviewed.

Consider an indenter with a given geometry $h = h(r, \vartheta)$, with r and ϑ polar coordinates. The previous models [20, 21] assume that plastic deformation of the surface is accompanied by the generation of sub-surface geometrically necessary dislocation loops (supposed to be of length $l(h)$ in this treatment). The deformation volume (V) is assumed to be a hemispherical zone below the projected area (A) of the indentation impression, with radius $a = \sqrt{A/\pi}$ (Fig. 6.14). Its value can be obtained by:

$$V = 2\pi/3(A/\pi)^{3/2} \tag{6.1}$$

Thus, the total length L of the geometrically necessary dislocation loops can be evaluated by summating the number of steps on the staircase-like indented surface (Fig. 6.14):

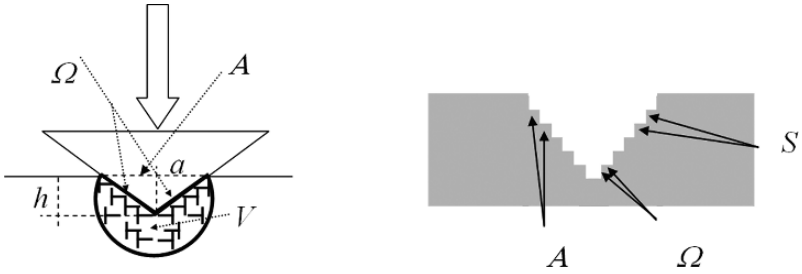

Fig. 6.14. Geometrically necessary dislocations during indentation: h is the indentation depth; a is the radius of the projected area A; Ω is the contact area and V is the dissipation domain (proportional to a^3). Note that the indented surface at the nanoscale appears in discrete steps due to the formation of dislocation loops, i.e., of quantized plasticity. In our model, the scaling law is predicted to be a function only of S/V, where $S = \Omega - A$. [Reprinted from [28], Copyright (2006), with permission from Elsevier.]

$$L = \sum_{steps} l_i = \frac{\Omega - A}{b} = \frac{S}{b} \approx \frac{1}{b} \int_0^h l(h)\mathrm{d}h \tag{6.2}$$

where Ω is the contact area of the indented zone and b is (modulus of the) Burger's vector. Considering that the indented surface at the nanoscale appears in discrete steps due to the formation of dislocation loops, Ω can be defined as the sum of the "vertical" surfaces (S) and of the "horizontal" ones (A – Fig. 6.14). Thus, the surface S can be interpreted as the total surface through which the energy flux arises, positive if outgoing (Ω) and negative if incoming (A) in the indenter. Note the generality of the result in Eq. (6.2), which does not need any specification of the form of h, as usually required.

According to Eq. (6.2), the average geometrically necessary dislocation density is:

$$\rho_G = \frac{L}{V} = \frac{S}{bV} \tag{6.3}$$

while the total dislocation density is usually assumed to be:

$$\rho_T = \bar{r}\rho_G + \rho_S \tag{6.4}$$

Where $\bar{r}\rho_G$ can be considered as the actual number of dislocations that must be generated to accommodate plastic deformation, that we could call geometrically "sufficient" dislocations, and it is greater than the number of geometrically necessary dislocations ρ_G [34] by the so-called Nye factor $\bar{r}$ (~ 2, [21]). ρ_S is the statistically stored dislocation density [20]. However, we note here that, according to Eq. (6.4), $\rho_T(V/(bS) \to 0) \to \infty$, i.e., the total dislocation density at the nanoscale diverges, whereas it must physically present a finite upper-bound, which we call $\rho_T^{(\mathrm{nano})}$. The existence of such an upper-bound has recently been confirmed [28, 35].

Note that ρ_T is related to the shear strength τ_p by the Taylor's hardening model [36], i.e.:

$$\tau_p = \alpha \mu b \sqrt{\rho_T} \tag{6.5}$$

where μ is the shear modulus and α is a geometrical constant usually in the range 0.3–0.6 for FCC metals [37]. Thus, the upper-bound $\rho_T^{(\text{nano})}$ is related to the existence of a finite nanoscale material strength $\tau_p^{(\text{nano})}$, that only at the true atomic scale is expected to be of the order of magnitude of the theoretical material strength.

Accordingly, the upper-bound $\rho_T^{(\text{nano})}$ is straightforwardly introduced in our model through the following asymptotic matching:

$$\frac{1}{\rho_T} = \frac{1}{\bar{r}\rho_G + \rho_S} + \frac{1}{\rho_T^{(\text{nano})}} \tag{6.6}$$

Note that at the atomic scale, as a consequence of the quantized nature of matter, $\rho_T^{(\text{nano})}$ must be (at least theoretically) of the order of b^{-2} as for a pure single dislocation. This is also reflected in the fact that $\beta = 1/(b^2 \rho_T^{(\text{nano})}) = (\alpha\mu/\tau_p^{(\text{nano})})^2$ is of the order of the unity, since $\alpha\mu$ is of the same order of magnitude as the theoretical material strength. Note the analogy with Quantized Fracture Mechanics (QFM) [38] that, quantizing the crack advancement as must (particularly) be at the nanoscale, predicts a finite theoretical material strength, in contrast to the results of the continuum-based linear elastic fracture mechanics [39].

The flow stress is related to the shear strength by von Mises' rule, i.e. $\sigma_p = \sqrt{3}\tau_p$, and the hardness is related to the flow stress by Tabor's factor [40], i.e., $H = 3\sigma_p$ [20, 21]; thus $H = 3\sqrt{3}\tau_p$. Introducing in this equation the shear strength given by Eq. (6.5), after having substituted the total and geometrically necessary dislocation densities according to Eq. (6.6) and Eq. (6.3) respectively, we derive $H = 3\sqrt{3}\alpha\mu b \left\{ (\bar{r}S/(bV) + \rho_S)^{-1} + \left(\rho_T^{(\text{nano})}\right)^{-1} \right\}^{-1/2}$. Finally, rearranging this relation and introducing dimensionless parameters, we deduce the following hardness scaling law [28]:

$$\frac{H(S/V)}{H_{\text{nano}}} = \left(\frac{\delta^2 - 1}{\ell S/V + 1} + 1 \right)^{-1/2}, \frac{H(S/V)}{H_{\text{macro}}} = \left(\frac{\delta^2 - 1}{\delta^2 V/(\ell S) + 1} + 1 \right)^{1/2},$$

$$\delta = \frac{H_{\text{nano}}}{H_{\text{macro}}} \tag{6.7}$$

where

$$H_{\text{nano}} \equiv H(\ell S/V \to \infty) = 3\sqrt{3/\beta}\alpha\mu$$

$$H_{\text{macro}} \equiv H(\ell S/V \to 0) = \frac{3\sqrt{3}\alpha\mu b}{\sqrt{\rho_S^{-1} + \beta b^2}}$$

$$\ell = \frac{\bar{r}}{\rho_S b}$$

H_{macro} represents the macro-hardness, H_{nano} the nano-hardness, and ℓ a characteristic length, governing the transition from nano- to macro-scale. From a physical point of view note that $\ell S/V = \bar{r}\rho_G/\rho_S$, i.e., it is equal to the ratio of the geometrically "sufficient" and statistically stored dislocation densities, whereas $\delta = \sqrt{1 + \rho_T^{(\text{nano})}/\rho_S}$. The two equivalent expressions in Eq. (6.7) correspond respectively to a bottom-up view or to a top-down view. Equation (6.7) is a general shape/size-effect law for nanoindentation that provides the hardness as a function of the ratio between the net surface through which the energy flux propagates and the volume where the energy is dissipated; or, simply stated, as a function of the surface over volume ratio of the domain where the energy dissipation occurs.

The law of Eq. (6.7) can be applied in a very simple way to treat any interesting indenter geometry. However, to make a comparison, it is useful to focus on the axisymmetric profiles (i.e., $h = h(r)$), yet to be investigated by other researchers [21].

Conical indenter. Considering a conical indenter with corner angle φ, its geometry will be defined by: $h(r) = \tan((\pi - \varphi)/2)r$; thus by integration with Eq. (6.2) we found $S/V = \frac{3\tan^2((\pi-\varphi)/2)}{2h}$, which can be introduced into Eq. (6.7), giving the following expression:

$$H_{\text{cone}}(h, \varphi) = H_{\text{macro}}\sqrt{1 + \frac{\delta^2 - 1}{\delta^2 h/h^*(\varphi) + 1}} \tag{6.8}$$

where

$$h^*(\varphi) = 3/2\ell \tan^2((\pi - \varphi)/2)$$

From physical considerations about Eq. (6.8), we can observe that, for $h/h^* \to 0$ or $\varphi \to 0$, $H_{\text{cone}} \to H_{\text{nano}}$, whereas for $h/h^* \to \infty$ or $\varphi \to \pi$, $H_{\text{cone}} \to H_{\text{macro}}$; only for the case of $\delta \to \infty$ (which means that $H_{\text{cone}} \to H_{\text{nano}} = \infty$ for $h \to 0$), $H_{\text{cone}} = H_{\text{macro}}\sqrt{1 + h^*/h}$ as derived by Nix et al. [20] (with the identical expression for $h^*(\varphi)$). Note that such a scaling law was previously proposed by Carpinteri [41] for material strength (with h structural size).

We have here derived S by integration of $l(h)$, according to Eq. (6.2) and for consistency with Swadener et al. [21]. A more direct calculation considers the difference between the lateral (Ω) and base (A) surface areas of Eq. (6.2), leading to a slightly different value of h^* [$h^*(\varphi) = 3/2\ell \tan^2((\pi - \varphi)/2)(1/\sin((\pi - \varphi)/2)) - 1/\tan((\pi - \varphi)/2)$]; with respect to the calculated previous one [$h^*(\varphi) = 3/2\ell \tan^2((\pi - \varphi)/2)$]. The ratios $h^*(\varphi)/\ell$ evaluated with the two different procedures were compared in [28] for a conical indenter: the related difference was moderate and unessential in our context. Thus, we conclude that both the methodologies can be applied to fit experiments.

Parabolic (spherical) indenter. Consider the case of a parabolic indenter with radius at tip R, i.e., $h = r^2/(2R)$, that for not too large an indentation depth

corresponds also to the case of a spherical indenter. By integration we found $S/V = 1/R$, that introduced into Eq. (6.7) gives:

$$H_{\text{parabola}}(R) = H_{\text{macro}}\sqrt{1 + \frac{\delta^2 - 1}{\delta^2 R/R^* + 1}} \tag{6.9}$$

where

$$R^* = \ell$$

Thus, the hardness is here not a function of the indentation depth h. We can observe that for $R/R^* \to 0$, $H_{\text{parabola}} = H_{\text{nano}}$, whereas for $R/R^* \to \infty$, $H_{\text{parabola}} = H_{\text{macro}}$; only for the case of $\delta \to \infty$, $H_{\text{parabola}} = H_{\text{macro}}\sqrt{1 + R^*/R}$, as derived in [21] (with the identical expression for R^*). This law describes a true size-effect and agrees with the Carpinteri's law [41].

Conical indenter with a rounded tip. Assuming the presence of a non-vanishing tip radius of curvature (R) in a conical indenter, the tip geometry that we consider in order to find a theory which models this kind of problem is the one reported in Fig. 6.15 [29]. Note that geometrically $h_S = R(1 - \sin\varphi)$, $h_C = R(1 - \sin\varphi)/\sin\varphi$ and r depends on the depth of indentation (h) and it is: $r = \sqrt{2Rh - h^2}$ for $h \le h_S$ or $r = (h + h_C)\tan\varphi$ for $h > h_S$.

Thus, the term $\frac{S}{V}(h, \varphi, R)$ can be deduced as a function of h, φ, and also R, by geometrical consideration as [29]:

$$\frac{S}{V}(h, \varphi, R) = \begin{cases} \dfrac{3h^2}{2(2Rh - h^2)^{3/2}} & h \le h_S \\ \dfrac{[(h + h_C)^2 - (h_S + h_C)^2](1/\sin\varphi - 1)\tan^2\varphi + h_S^2}{2/3 \cdot (h + h_C)^3 \tan^3\varphi} & h > h_S, \end{cases} \tag{6.10}$$

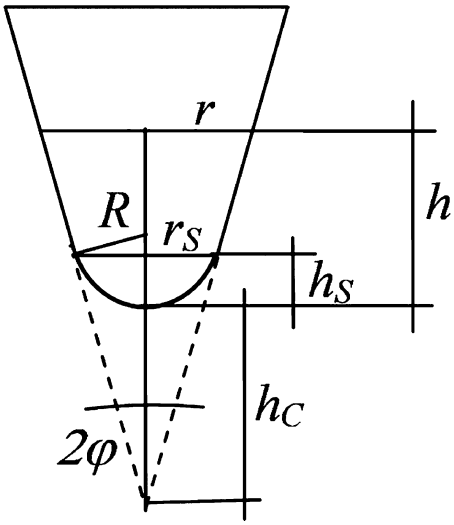

Fig. 6.15. Conical indenter with worn spherical tip [29]

Introducing Eq. (6.10) into Eq. (6.7) it is possible to have an expression for the material hardness as a function of: (1) depth of indentation, (2) tip corner angle, (3) tip radius of curvature ($H(h, \varphi, R)$).

Note the continuity of the function $S/V(h, \varphi, R)$ around h_S and note that $S/V(h >> R, \varphi, R) \equiv S/V(h, \varphi, R = 0)$. This means that the role of the tip radius of curvature becomes negligible for large indentation depths (in agreement with the macro-scale results). Obviously S/V ($h \leq h_S, \varphi, R$) is not a function of φ, just representing a pure spherical indentation.

Imagine performing experiments with an ideal tip (thus with $R \to 0$), in order to measure the ideal material hardness $H_{\text{ideal}} \equiv H(h, \varphi, R = 0)$. Unfortunately, we would experimentally measure $H_{\text{measured}} \equiv H(h, \varphi, R_{\text{exp}})$ and thus the ideal material hardness will be $H_{\text{ideal}} = CH_{\text{measured}}$, thus the correction factor C will be defined as [29]:

$$C = \frac{H(h, \varphi, R = 0)}{H(h, \varphi, R_{\text{exp}})} \tag{6.11}$$

Since $S/V(h, \varphi, R)$ Eq. (6.10) increases by decreasing R, correction factors C larger than one have to be expected ($C \geq 1$). For this reason, wear would imply hardness underestimations, in agreement with the finite element results (see Fig. 6.20a).

In particular introducing Eq. (6.7) and Eq. (6.10) into Eq. (6.11) gives:

$$C(h, \varphi, R) = \sqrt{\frac{1 + \dfrac{\delta^2 - 1}{\delta^2 \ell^{-1} V/S(h, \varphi, 0) + 1}}{1 + \dfrac{\delta^2 - 1}{\delta^2 \ell^{-1} V/S(h, \varphi, R_{\text{exp}}) + 1}}} \tag{6.12}$$

which allows us to deduce the correction factors C for the nanofabricated probes used for the experimental part of this work (Sects. 6.2.1 and 6.2.2). The values of the correction factors are reported in Table 6.5 [29].

Flat indenter. Consider the case of a flat indenter of radius a, geometrically we found $S/V = \frac{2\pi ah}{2/3\pi a^3}$, that introduced into Eq. (6.7) gives:

$$H_{\text{flat}}(a, h) = H_{\text{macro}} \sqrt{1 + \frac{\delta^2 - 1}{\delta^2 \, a^2/(3h\ell) + 1}} \tag{6.13}$$

For $a/\ell \to 0$, $H_{\text{flat}} \to H_{\text{nano}}$, whereas for $a/\ell \to \infty$, $H_{\text{flat}} \to H_{\text{macro}}$; interestingly, for $h/\ell \to 0$, $H_{\text{flat}} \to H_{\text{macro}}$, whereas for $h/\ell \to \infty$, $H_{\text{flat}} \to H_{\text{nano}}$, showing an inverse h-size-effect, in agreement with the discussion by Swadener

Table 6.5. Tip radius of curvature correction factors for the nanofabricated probes [29]

Indenter	Correction factor (C)
Probe n°1 ($R = 21$, nm, $\varphi = 62°$)	1.156
Probe n°2 ($R = 24$, nm, $\varphi = 97°$)	1.840
Probe n°3 ($R = 26$, nm, $\varphi = 25°$)	1.036

et al. [21] and with intuition (the contact area does not change when the penetration load or depth increase) [24]. This suggests a new intriguing methodology to derive the nanoscale hardness of materials by a macroscopic experiment, using large flat punches, even if the finite curvature at the corners is expected to affect the results. This case was only discussed in [21], because of the complexity in their formalism to treat such a cuspidal geometry. Note that for $h \propto a$ and $\delta \to \infty$ the size-effect law again coincides with that introduced by Carpinteri [41].

6.5 Deconvolution of the Indentation Impressions

The presence of a radius of curvature at the tip in an AFM indenter, affects not only the process of indentation, but also the process of AFM imaging, as long as the non-ideal tip interacts with the morphology, convoluting the asperities depending on its actual shape. For this reason, in order to deal with this problem, which could dramatically influence the AFM hardness results, the AFM images have been geometrically deconvoluted [29], considering the tip radius of curvature that we measured during the topography characterization (Sect. 6.2.2).

The software that we used to measure the indentation impression area (SPIP™ software), considers a "tangent height" of the indentation (which is the depth of indentation) reduced by 10%, in order to avoid any roughness influence (see Fig. 6.16a where h is 10% of the whole depth of indentation H). In Fig. 6.16a the red dashed line is the artifact image obtained by AFM, assuming the presence of a tip radius of curvature R, while the black continuous line is the ideal profile. Thus, considering the "tangent height," the difference between the measured indentation impression and the ideal one is only related to the length x (Fig. 6.16a,b, [29]), which could be obtained by geometrical considerations as $x = R \cdot \cos\alpha$, with $\alpha = \text{arcsen}\left(1 - \frac{h}{R}\right)$.

The actual projected area (A^I – hatched area in Fig. 6.16b) could be thus obtained from the measured one (A_p – pink area in Fig. 6.16b) with the following relation:

$$A^I = \frac{\sqrt{3}}{4} \cdot \left(\sqrt{\frac{4 \cdot A_p}{\sqrt{3}}} + 2 \cdot \sqrt{3} \cdot x \right) \tag{6.14}$$

6.6 Results

The nanohardness was first calculated following the Oliver–Pharr approach [8, 9, 11, 19], analyzing the load-unload curves performed during the experimental campaign. In this case the material is highly deformable in the plastic regime and a huge pile-up occurs. For this reason the hardness value will be extremely overestimated using the O-P method. In some cases the material that piles up aside the indentation, almost doubles the indentation depth. This means that the projected area

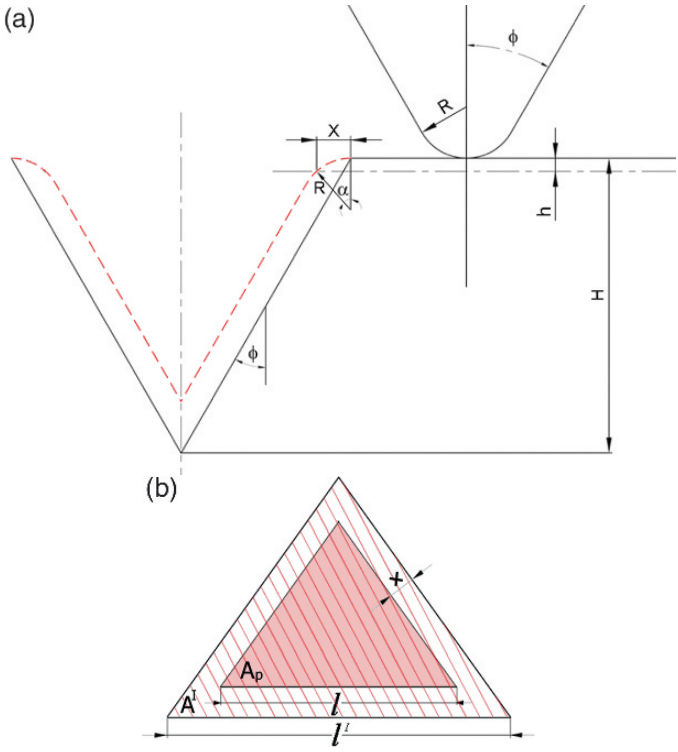

Fig. 6.16. Schematic of the deconvolution process; **a** interaction during the AFM imaging phase between the tip and the indentation impression; **b** projected area of the indentation impression [29]

(which is proportional to h^2) should be approximately four times larger and the hardness value four times smaller than the O-P values [19].

For this reason we adopted a direct method to measure the projected area of the indentation impression (Sect. 6.2.3). The hardness results obtained in this way are reported in Fig. 6.17 (blue dots) where a higher statistic has been obtained in comparison with the results shown in [19], increasing the number of indentations on the same material [29]. With a direct measurement of the projected area it is possible to take into account the pile-up effect. In the legend the best-fit parameters obtained with the theoretical model described in Sect. 6.4 for a conical indenter, are reported. The macro-hardness (H_{macro}) appears quite similar to the actual value of the polymer material and also the other best-fit parameters are plausible and this confirms that the theoretical model is self-consistent.

As introduced in Sect. 6.3, a FEM simulation has been performed. This numerical approach allowed us to verify the experimental results and to understand better how the indenter shape affects the hardness measurement. As a matter of fact, the study of the distribution of pressure in the contact area between the specimen and the indenter, could provide several useful pieces of information [19].

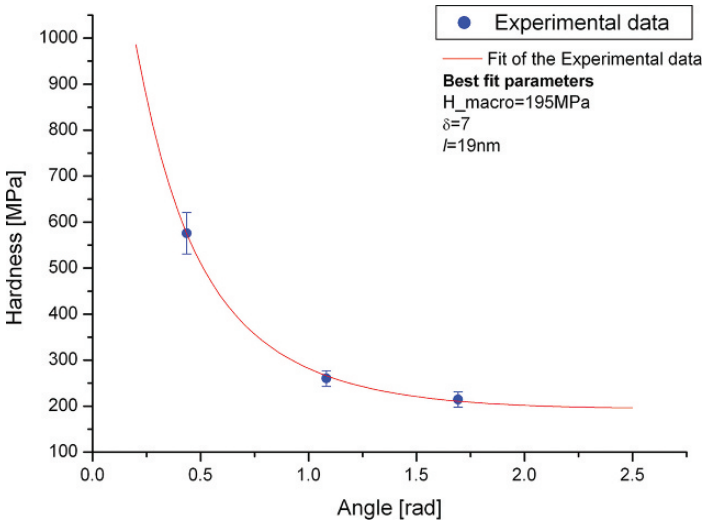

Fig. 6.17. Experimental results (*blue dots*) for the three customized indentation probes obtained with a direct measurement of the projected area and theoretical interpolation (*red line*)

In Fig. 6.18 the numerical hardness results are reported for the range of angles under study. The corner angle 2_{φ} assumes the following values for the three probes investigated (Table 6.2): 25° (0.436 rad), 62° (1.082 rad), 97° (1.693 rad).

In Fig. 6.19 [29] a direct comparison between the experimental and numerical results is reported. This comparison reveals a good agreement in the hardness

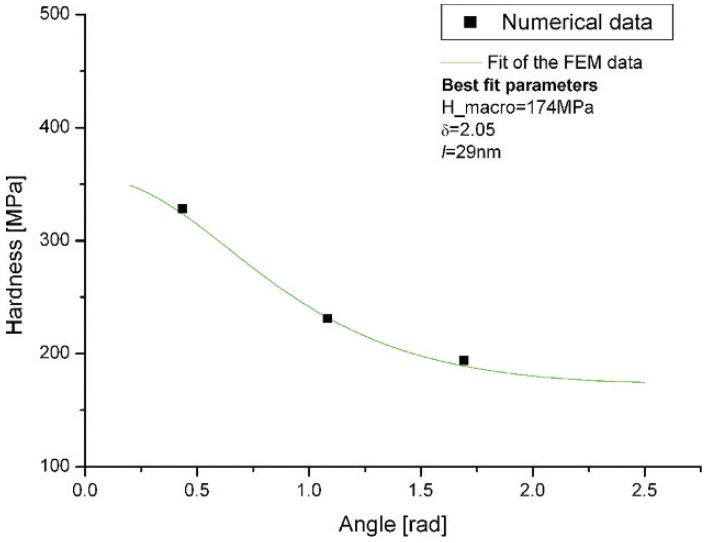

Fig. 6.18. Numerical results (*black squares*) for the indentation model over the whole range of the indenter corner angles and theoretical interpolation (*green line*)

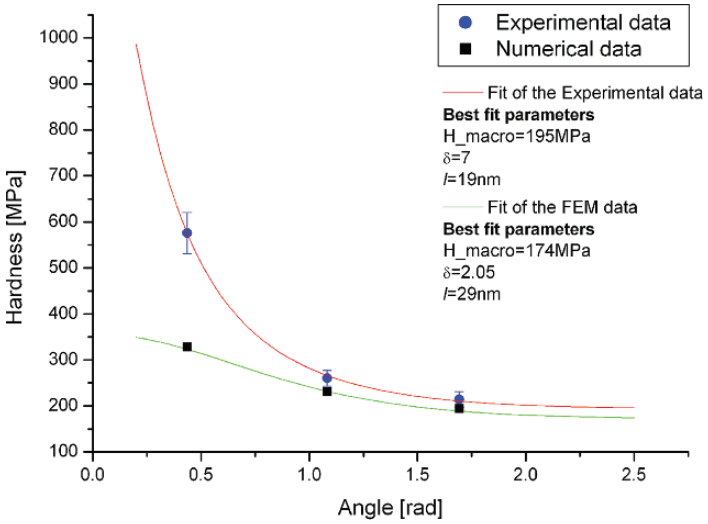

Fig. 6.19. Comparison between the experimental and numerical results, both interpolated using the "general size/shape-effect law for nanoindentation" [29]

behavior although an overestimation of the experimental results is evident at small corner angles as a consequence of the tip radius of curvature effect. We should thus expect that the presence of a rounded tip on the indenter gives an overestimation of the measured hardness, justifying the gap between experimental and numerical results, observable in the graph. On the contrary, as highlighted from numerical simulations (Fig. 6.20a) and confirmed from theoretical models (Sect. 6.4 – *Conical indenter with a rounded tip*), the effect of the tip radius of curvature on the hardness measurement in terms of penetration process is opposite. The hardness value, numerically evaluated modeling the indenter as ideal (Fig. 6.20a – red dots), is in fact higher than that evaluated using a worn tip (Fig. 6.20a – blue squares). These numerical data have also been fitted with the theoretical Eqs. (6.7, 6.10), considering in the first case (red curve) a vanishing tip radius ($R = 0$) while in the second case (blue curve) the actual tip radii of the three customized probes is considered (Table 6.3). The best fit parameters reported in the inset of Fig. 6.20a have exactly the same values for the two interpolations, confirming that the theoretical approach perfectly agrees with the numerical one.

The mismatch observed in Fig. 6.19 is therefore not ascribable to the tip radius of curvature effect on the indentation process, but it is ascribable to this effect on the AFM imaging process. As reported in Sect. 6.5, in fact, the measured projected area of an indentation impression is slightly smaller than the real one, because of the convolution effect of the AFM tip. Thus, considering this effect and correcting the measured areas with the procedure described in Sect. 6.5, we are able to estimate the actual value of the material hardness. In Fig. 6.20b [29] raw experimental data (green triangles) vs. deconvoluted experimental data (magenta triangles) are reported. It is possible to observe the difference, especially for small corner angles, in the hardness values. In the same

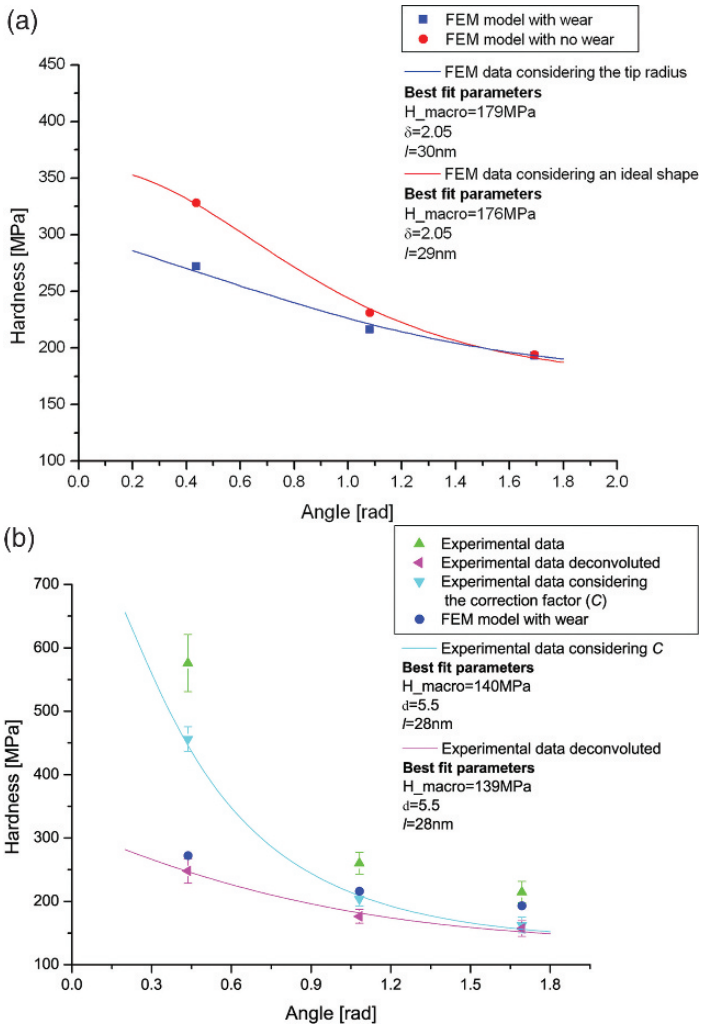

Fig. 6.20. (**a**) Numerical hardness results considering in the FEM model an indenter with an ideal shape (*red dots*) and with a worn shape (*blue squares*). The numerical data are theoretically interpolated (*red* and *blue line*, respectively); (**b**) comparison between the experimental results deconvoluted (*magenta triangles*) and numerical data (*blue dots*). In the same graph are also reported the raw experimental results (*green triangles*) and the experimental results considering the correction factor *C* (*cyan triangles*) [29]

graph the numerical data of the modeled worn indenter are also reported, showing now an excellent agreement along the whole range of the corner angles chosen. Lastly, we also filtered the deconvoluted experimental results (magenta triangles) by the correction factor *C*, theoretically evaluated for the three customized probes (Table 6.5). These corrected data are also reported in Fig. 6.20b

(cyan triangles). The results filtered by the deconvolution process (magenta triangles) and those corrected by the correction factor *C* (cyan triangles) have both been theoretically interpolated (magenta and cyan curve, respectively). The result of this process reveals a complete agreement in terms of best-fit parameters (inset of Fig. 6.20b), which are exactly the same, confirming that the theoretical model is self-consistent [29].

6.7 Conclusion

An AFM-based nanoindentation study on the effect of geometrical uncertainties of the indenter tip on the hardness measurement is proposed herein. In particular three different-shaped indentation probes have been designed and realized with a FIB machine. A whole experimental analysis has been performed with these indenters in order to quantify how the hardness measurement is affected by two important parameters: (1) the tip corner angle [19] and (2) the tip radius of curvature of the nanoindenters [29]. A FEM model has also been designed in order to better understand the process of indentation and it has been further developed in order to take into account the tip radius of curvature effect. In parallel, a theoretical approach, based on a recent theory on nanoindentation [28], has been optimized for a worn indenter. These two approaches allow us to interpret the experimental results, showing that the differences between the experimental, the numerical, and the theoretical data are related mainly to the tip radius of curvature effect, which affects not only the penetration process during indentation, but also, and in a significant way, the AFM imaging process. The hardness has been in fact obtained in a direct way, measuring the projected area of the indentation impression by the AFM high-resolution images. A geometrical deconvolution process has been utilized in order to correct the systematic error related to the tip radius of curvature effect.

In this way it is possible to deduce a theoretical relation that links the measured hardness value with the shape of the indenter and with its tip radius of curvature. In particular a correction factor *C* has been defined and it allows us to correct the experimental data, obtained by AFM nanoindentation, from the geometrical effects of the indenter tip.

Acknowledgments. The authors would like to acknowledge the FIB laboratory (a CNR-INFM-S3 Lab).

This work has been supported by Regione Emilia Romagna (LR n.7/2002, PRRIITT misura 3.1A) and Net-Lab SUP&RMAN (Hi-Mech district for Advanced Mechanics Regione Emilia Romagna).

The author Nicola Pugno was supported by the "Bando Ricerca Scientifica Piemonte 2006" – BIADS: Novel biomaterials for intraoperative adjustable devices for fine tuning of prostheses shape and performance in surgery.

References

1. Fischer-Cripps AC (2004) Nanoindentation. Springer, New York
2. Li X, Bhushan B (2002) A review of nanoindentation continuous stiffness measurement technique and its applications. Mater Charact 48(1):11–36
3. Saha R, Nix WD (2002) Effects of the substrate on the determination of thin film mechanical properties by nanoindentation. Acta Mater 50(1):23–38
4. Zhang F, Saha R, Huang Y, Nix WD, Hwang KC, Qu S, Li M (2007) Indentation of a hard film on a soft substrate: strain gradient hardening effects. Int J Plasticity 23:25–43
5. Bhushan B, Koinkar VN (1994) Nanoindentation hardness measurements using atomic force microscopy. Appt Phys Lett 64(13):1653–1655
6. Bhushan B (2004) Handbook of nanotechnology. Springer, Berlin
7. Doerner MF, Nix WD (1986) A method for interpreting the data from depth-sensing indentation instruments. J Mater Res 1(4):601–109
8. Oliver WC, Pharr GM (1992) An improved technique for determining hardness and elastic modulus using load and displacement sensing indentation experiments. J Mater Res 7(6):1564
9. Oliver WC, Pharr GM (2004) Measurement of hardness and elastic modulus by instrumented indentation: advances in understanding and refinements to methodology. J Mater Res 19(1):3–20
10. VanLandingham MR (2003) Review of Instrumented Indentation. J Res Natl Inst Stand Technol 108:249–265
11. Pharr GM, Oliver WC, Brotzen FR (1992) On the generality of the relationship among contact stiffness, contact area, and elastic modulus during indentation. J Mater Res **7**(3):613–617
12. Withers JR, Aston DE (2006) Nanomechanical measurements with AFM in the elastic limit. Adv Colloid Interface 120(1–3):57–67
13. VanLandingham MR, Villarrubia JS, Guthrie WF, Meyers GF (2001) Nanoindentation of polymers: An Overview, Macromol. Symp. 167. In: Tsukruk VV, Spencer ND (eds) Advances in scanning probe microscopy of polymers. Wiley-VCH Verlag GmbH, Weinheim, Germany, pp 15–43
14. Beegan D, Chowdhury S, Laugier MT (2005) Work of indentation methods for determining copper film hardness. Surf Coat Technol 192:57–63
15. Miyake K, Fujisawa S, Korenaga A, Ishida T, Sasaki S (2004) The effect of pile-up and contact area on hardness test by nanoindentation. Jpn J Appl Phys 43(7B) 4602–4605
16. Poole WJ, Ashby MF, Fleck NA (1996) Micro-hardness of annealed and work-hardened copper polycrystals. Scr Mater 34(4):559–564
17. Pharr GM (1998) Measurement of mechanical properties by ultra-low load indentation. Mater Sci Eng A 253(1–2):151–159
18. Saha R, Xue Z, Huang Y, Nix WD (2001) Indentation of a soft metal film on a hard substrate: strain gradient hardening effects. J Mech Phys Solids 49(9):1997–2014
19. Calabri L, Pugno N, Rota A, Marchetto D, Valeri S (2007) Nanoindentation shape-effect: experiments, simulations and modelling. J Phys: Condens Matter 19:395002–395013
20. Nix WD, Gao H (1998) Indentation size effects in crystalline materials: a law for strain gradient plasticity. J Mech Phys Solids 46:411–425
21. Swadener JG, George EP, Pharr GM (2002) The correlation of the indentation size effect measured with indenters of various shapes. J Mech Phys Solids 50:681–694
22. VanLandingham MR (1997) The effect of instrumental uncertainties on AFM indentation measurements. Microscopy Today 97:12–15
23. Mott BW (1956) Micro-indentation hardness testing. Butterworths, London

24. Ashby MF (1970) The deformation of plastically non-homogenous materials. Philos Mag 21:399–424
25. Nye JF (1953) Some geometric relations in dislocated crystals. Acta Metall 1:153–162
26. Poole WJ, Ashby MF, Fleck NA (1996) Micro-hardness tests on annealed and work-hardened copper polycrystals. Scripta Mater 34:559–564
27. Lim YY, Chaudhri MM (1999) The effect of the indenter load on the nanohardness of ductile metals: an experimental study on polycrystalline work-hardened and annealed oxygen-free copper. Philos Mag A 79:2879–3000
28. Pugno N (2006) A general shape/size-effect law for nanoindentation. Acta Materialia 55:1947–1953
29. Calabri L, Pugno N, Menozzi C, Valeri S (2008) AFM nanoindentation: tip shape and tip radius of curvature effect on the hardness measurement. J Phys: Condens Matter (unpublished)
30. Sader JE, Chon JWM, Mulvaney P (1999) Calibration of rectangular atomic force microscope cantilevers. Rev Sci Instrum 70:3967–3969
31. Sader JE, Larson I, Mulvaney P, White LR (1995) Method for the calibration of atomic force microscope cantilevers. Rev Sci Instrum 66:3789–3798
32. Bhattacharya AK, Nix WD (1988) Finite element simulation of indentation experiments. Int J Solids Struct 24:881–891
33. Yoshimoto K, Stoykovich MP, Cao HB, de Pablo JJ, Nealey PF, Drugan WJ (2004) A two-dimensional model of the deformation of photoresist structures using elastoplastic polymer properties. J Appl Phys 96:1857–1865
34. Arsenlis A, Parks DM (1999) Crystallographic aspects of geometrically-necessary and statistically-stored dislocation density. Acta Mater 47:1597–1611
35. Huang Y, Zhang F, Hwang KC, Nix WD, Pharr GM, Feng G (2006) A model of size effects in nano-indentation. J Mech Phys Solids 54:1668–1686
36. Taylor GI (1938) Plastic strain in metals. J Inst Met 13:307–324
37. Wiedersich H (1964) Hardening mechanisms and the theory of deformation. J Met 16:425–430
38. Pugno N, Ruoff R (2004) Quantized fracture mechanics. Philos Mag 84/27:2829–2845
39. Griffith AA (1920) The phenomena of rupture and flow in solids. Phil Trans Roy Soc A 221:163–199
40. Tabor D (1951) The hardness of metals. Clarendon Press, Oxford
41. Carpinteri A (1994) Scaling laws and renormalization groups for strength and toughness of disordered materials. Int J Solids Struct 31:291–302